Journal of Solid State Electrochemistry
https://doi.org/10.1007/s10008-023-05409-w

ORIGINAL PAPER

Electrochemical behavior of perovskite-type $Ce_{1-x}Ca_xVO_3$ under reducing conditions

E. V. Tsipis[1] · D. V. Zhigacheva[1] · A. O. Zhigachev[1] · O. F. Shakhlevich[1] · S. I. Bredikhin[1] · V. V. Kharton[1]

Received: 29 November 2022 / Revised: 17 January 2023 / Accepted: 23 January 2023

Abstract

The incorporation of calcium into the zircon-type lattice of $Ce_{1-x}Ca_xVO_4$ ($x = 0.2$–0.4), stable at atmospheric oxygen pressure, leads to a modest decrease in the unit cell volume and electrical conductivity, predominantly electronic. The average linear thermal expansion coefficients (TECs) of vanadate ceramics in air vary in the range $(6.6–9.9)\times10^{-6}$ K^{-1} at 393–1123 K, increasing with temperature and x. On reduction in hydrogen, zircon-type $Ce_{1-x}Ca_xVO_4$ undergoes phase transformation into perovskite-like $Ce_{1-x}Ca_xVO_3$. This transition is accompanied by a 32% crystal lattice contraction and a drastic increase in the conductivity, up to 120 S/cm at 1123 K for $Ce_{0.6}Ca_{0.4}VO_3$. The average TECs of reduced metavanadates, $(9.7–12.7)\times10^{-6}$ K^{-1} at 393–1123 K, are compatible with those of solid oxide electrolytes. As for the variations of electronic resistivity, the polarization resistance of porous $Ce_{1-x}Ca_xVO_3$ electrodes in reducing atmospheres decreases with calcium additions. The electrochemical activity of $Ce_{1-x}Ca_xVO_3$ in contact with zirconia-based electrolyte, and protective ceria interlayer is higher for H_2O electrolysis with respect to H_2 oxidation.

Keywords Cerium vanadate · SOFC/SOEC electrode · Electronic conductivity · Thermal expansion · Phase transition

Introduction

Important advantages of solid oxide fuel cells (SOFCs) include relatively low requirements for fuel purity and an ability to operate using various types of gaseous fuels, including light hydrocarbons. Hydrogen sulfide, being a component of associated petroleum gases and natural gas, may however induce serious problems for the SOFC operation. The presence of H_2S even in small amounts (at the ppm level) causes catalytic poisoning and corrosion of nickel-based cermet anodes ([1–4] and references therein). In order to minimize irreversible degradation of the anode, additional purification of the fuels from H_2S is usually required. At the same time, taking into account the relatively high costs of desulfurization, direct use of the fuels with substantial sulfur concentrations seems more attractive. Another serious challenge associated with the direct electrochemical oxidation of hydrocarbons in SOFCs refers to the carbon deposition on Ni-containing anodes. The latter problem is also relevant for the cathodes of solid oxide electrolysis cells (SOECs) during CO_2 electrolysis.

Oxide phases based on perovskite-type $CeVO_3$ having unique electrical and catalytic properties in reducing environments, are often considered promising for the SOFC anode components tolerant to the presence of H_2S and other sulfur-containing compounds [4–10]. As for doped lanthanum vanadates, these materials possess an essentially high catalytic activity towards electrochemical oxidation of H_2S [2–4]. Cerium metavanadate $CeVO_3$ can be prepared by reduction of $CeVO_4$ orthovanadate with the zircon-type structure stable in air [8, 9, 11], where the prevailing oxidation states of cerium and vanadium cations are 3 + and 5 +, respectively [12]. Pure $CeVO_3$, where the main oxidation state of vanadium is 3 +, does not exhibit reverse transformation back into $CeVO_4$ on further reoxidation; on the contrary, for Ca-doped $Ce_{1-x}Ca_xVO_4$ at $x \geq 0.2$, this phase transition is reversible on redox cycling without formation of impurity phases [9, 13]. The incorporation of bivalent cations, such as Ca^{2+} or Sr^{2+}, in $CeVO_4$ leads to a crystal lattice contraction and to increasing total conductivity [5, 7–9, 13–15]. For Ca^{2+} and Sr^{2+}, the solubility limits in $CeVO_4$ were determined as 41–57 and 17.5–37 mol.%, respectively [5, 7, 14, 15]. At atmospheric oxygen pressure, $Ce_{1-x}Ca_xVO_4$

✉ E. V. Tsipis
tsipis@issp.ac.ru

[1] Osipyan Institute of Solid State Physics, Russian Academy of Sciences, 142432 Chernogolovka, Russia

Published online: 01 February 2023

are mixed conductors with dominating electronic conductivity and oxygen-ionic transport via interstitial mechanism [8, 9]. The ion transference numbers of $Ce_{1-x}Ca_xVO_4$ ($x = 0$–0.2) vary in the range $(0.2–5.6)\times10^{-3}$ at 973–1223 K, increasing with temperature [8, 9]. The acceptor-doped cerium vanadates in air were reported oxygen deficient [7, 15] or slightly oxygen-hyperstoichiometric [5, 8, 14]. One should note that literature data on the solubility limits of alkaline-earth cations in $Ce_{1-x}A_xVO_4$, on the total electrical conductivity under both oxidizing and reducing conditions, as well as on the oxygen nonstoichiometry of these compounds, are quite contradictory.

Continuing previous studies of cerium vanadate-based materials [8, 9], the present work is focused on the assessment of functional properties of $Ce_{1-x}Ca_xVO_{3-\delta}$ ($x = 0.2$–0.4) as potential electrode materials and evaluation of their electrochemical activity in contact with stabilized zirconia solid electrolyte in the SOFC anode and SOEC cathode regimes.

Experimental section

Fine $Ce_{0.8}Ca_{0.2}VO_4$, $Ce_{0.7}Ca_{0.3}VO_4$, and $Ce_{0.6}Ca_{0.4}VO_4$ powders were synthesized via the nitrate-citrate route. The stoichiometric amounts of $Ce(NO_3)_3{\bullet}6H_2O$, $CaCO_3$, and NH_4VO_3 (99.9% purity) were dissolved in nitric acid with subsequent addition of citric acid. The molar amount of citric acid was 50% higher with respect to the stoichiometric citrate/nitrate ratio calculated assuming that the only gaseous products of reaction between nitrate ions and citric acid are H_2O, CO_2, and N_2. The solution was dried until self-ignition. The resultant powders were annealed at 773–1073 K in air for 40 h with several intermediate regrindings. Then these powders were uniaxially pressed into discs and sintered in air at 1373–1423 K for 5–10 h. The density of ceramics was 80–95% of the theoretical value, determined by the X-ray diffraction (XRD) results. The bar-shaped samples were cut from the sintered ceramics for the conductivity and dilatometric measurements. In order to verify the transition from zircon into perovskite structure, selected samples were annealed in flowing 5% H_2 – 3% H_2O—Ar gas mixture at 1123 K for 10 h and cooled down to room temperature in the same flow.

The XRD analysis of the powders and ceramics was carried out using a Rigaku SmartLab SE (CuK_α radiation). Static light scattering on an Analysette 22 NeXT nano laser particle sizer (Fritsch, Germany) was used to assess particle size distribution in the powders, preliminarily dispersed in bi-distilled water employing ultrasonic radiation. The microstructural analysis was performed by scanning electron microscopy coupled with energy dispersive spectroscopy (SEM/EDS) on a Supra 50VP (CarlZeiss, Germany) microscope. The thermal expansion behavior was studied using a vertical alumina dilatometer Linseis L75/N1 at heating/cooling rates of 3 K/min in flowing air or 5% H_2—Ar mixture. The total electrical conductivity was measured by the four-probe DC method (using Yokogawa GS200 DC voltage/current source and Fluke 8846A precision multimeter) on cooling in air or in flowing 5% H_2—Ar gas mixture humidified at room temperature. As the phase transition on reduction may be kinetically-stagnated [13], especially in the case of ceramic samples, prior to the conductivity and dilatometric measurements, the ceramics were equilibrated in flowing 5% H_2 – 3% H_2O—Ar gas mixture at 1123 K until the stable values of the sample resistance/length were obtained. In all other cases, the time necessary for conductivity stabilization after the temperature change was 30–60 min.

The electrochemical behavior was tested employing half-cells with vanadate working electrodes (WEs) and Pt counter and reference electrodes (CE and RE, respectively). The solid oxide electrolyte membranes of 10 mol.% Sc_2O_3, and 1 mol.% Y_2O_3 co-stabilized ZrO_2 (10Sc1YSZ) were pressed into discs (diameter of 27 mm), sintered in air at 1773 K for 10 h, and polished down to a thickness of 1.0 mm. The pastes containing $Ce_{1-x}Ca_xVO_4$ or $Ce_{0.9}Gd_{0.1}O_{1.95}$ (GDC10) were prepared by mixing of ball-milled powders with a V-006A binder (Heraeus, Germany). Porous WE layers (geometric area of 1.2 cm^2) were applied onto the electrolyte membranes by screen printing. In order to prevent chemical interaction between the electrode and electrolyte materials, a protective GDC10 interlayer was first deposited onto the solid electrolyte surface (screen #90, where the number indicates the number of threads per cm). Although XRD analysis revealed no secondary phases formed in the $Ce_{1-x}Ca_xVO_4$—10Sc1YSZ (50–50 wt/%) mixtures annealed in air at 1373 K for 10 h, the unit cell parameters of both phases were slightly changed after such thermal treatments, indicating possible cation interdiffusion. WEs were applied onto GDC10 interlayer by the same method (screen #43) in four steps with intermediate drying. The resulting electrodes were sintered in air at 1323–1373 K for 2 h. After sintering, the thicknesses of the protective interlayer and electrode layer were 8–10 and 20–25 μm, respectively; their sheet densities were 2 mg/cm^2 and 12 ± 1 mg/cm^2, correspondingly. Platinum RE (~ 1 mm in diameter) was placed at a distance of at least 6 mm from the WE. The produced half-cell was hermetically sealed on a holder using Kerafol glass sealant. Flowing 97% H_2 – 3% H_2O gas mixture (100 ml/min) and synthetic air were continuously supplied at the WE and CE, respectively. The oxygen partial pressure, $p(O_2)$, in the fuel chamber was monitored by an electrochemical zirconia sensor. The electrode overpotential (η) and polarization resistance (R_η) as a function of current density (i) were measured by the three-electrode technique in potentiostatic mode using

an Autolab 302N PGStat instrument equipped with FRA32 module (Metrohm Autolab, Netherlands) at 1123 K, as described elsewhere [10]. The values of ohmic and polarization resistances were determined from the impedance spectra collected in the frequency range from 0.1 Hz to 1 MHz.

Results and discussion

XRD analysis of $Ce_{1-x}Ca_xVO_4$ powders and sintered ceramics showed the formation of single phases with the zircon-type structure (space group $I4_1/amd$). Figure 1 displays selected examples of the powder XRD patterns; the unit cell parameters are listed in Table 1. The incorporation of Ca^{2+} leads to the lattice contraction confirming that acceptor-type doping is mainly charge-compensated by the formation of Ce^{4+} cations [9]. Note that the ionic radii of Ca^{2+} and Ce^{3+} in the same coordination (8 in the present case) are very close to one another [16]. The partial oxidation of Ce^{3+} into Ce^{4+} on calcium doping in $Ce_{1-x}Ca_xVO_4$ was also confirmed by X-ray photoelectron spectroscopy [17]. After annealing in 5% H_2 – 3% H_2O—Ar mixture at 1123 K and oxygen partial pressure ($p(O_2)$) of approximately 10^{-19} atm, the doped orthovanadates transform into metavanadates with the perovskite-type structure (space group *Pnma,* Fig. 2). Although the assumption [7] that these compositions are oxygen-stoichiometric seems rather doubtful, the presence of some V^{4+} fraction is considered reasonable taking into account the slight lattice contraction with increasing Ca^{2+} concentration (Table 1). The same conclusion can be drawn from the total conductivity variations discussed below. The transformation from orthovanadates to metavanadates is associated with $32 \pm 0.3\%$ volume contraction independent on the dopant concentration. This effect should be accounted when fabricating $Ce_{1-x}Ca_xVO_4$ electrodes; significant dimensional changes may cause cracking or even delamination of the electrode layers.

Figure 3 illustrates typical powder morphology (A) and ceramic microstructure (B) of the title materials, by the example of $Ce_{0.7}Ca_{0.3}VO_4$. The as-synthesized powders consisted of agglomerates of fine submicron- and micron-scale particles. Figures 4 and 5 display the particle size distribution assessed by the static light scattering technique. In all cases, the particle size distributions in as-prepared powders are clearly bimodal with the peak maxima at approximately 1 μm and 14–36 μm, depending on the composition. The latter peak is obviously attributed to the size of agglomerates. After ball-milling of the powders, the distributions

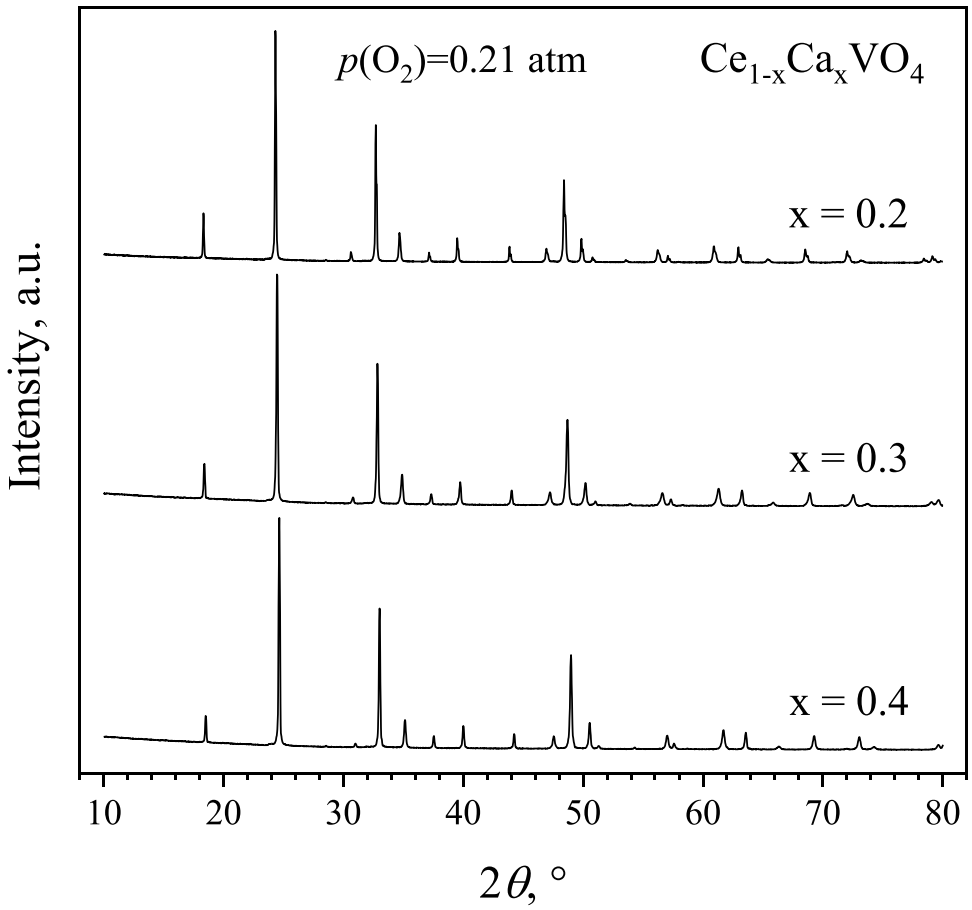

Fig. 1 XRD patterns of as-synthesized $Ce_{1-x}Ca_xVO_4$ powders after annealing in air at 1073 K

Table 1 Properties of $Ce_{1-x}Ca_xVO_{4\pm\delta}$ ceramics

x	Unit cell parameters		Average linear thermal expansion coefficient TEC × 10^6, K^{-1}			Activation energy for the total conductivity in air	
	$p(O_2)=0.21$ atm $I4_1/amd$	$p(O_2)=10^{-19}$ atm $Pnma$	T, K	Air	5% H_2-Ar	T, K	E_a, kJ/mol
0.2	$a=7.311$ Å $c=6.449$ Å $V=344.704$ Å^3	$a=5.504$ Å $b=7.716$ Å $c=5.482$ Å $V=234.082$ Å^3	393–853 853–1123	6.63 ± 0.04 7.49 ± 0.04	9.67 ± 0.07 11.08 ± 0.06	613–1173	37.3 ± 0.9
0.3	$a=7.262$ Å $c=6.419$ Å $V=338.517$ Å^3	$a=5.463$ Å $b=7.311$ Å $c=5.485$ Å $V=231.207$ Å^3	393–853 853–1123	7.36 ± 0.03 8.69 ± 0.03	10.73 ± 0.03 11.94 ± 0.04	773–1233	37.2 ± 0.8
0.4	$a=7.247$ Å $c=6.416$ Å $V=336.962$Å^3	$a=5.442$ Å $b=7.689$ Å $c=5.466$ Å $V=228.717$ Å^3	393–853 853–1123	7.91 ± 0.02 9.86 ± 0.05	11.44 ± 0.06 12.67 ± 0.03	723–1173	40 ± 1

became monomodal with the peak at approximately 0.7 μm; one example for $Ce_{0.7}Ca_{0.3}VO_4$ is presented in Fig. 5. As milling enables complete agglomerate destruction, the pastes for electrode layer screen-printing were made of the milled powders. The grain size in the sintered vanadate ceramics varied in the range from 1 to 8 μm.

Figure 6 shows the dilatometric curves of $Ce_{1-x}Ca_xVO_4$ ceramics on cooling in air and in flowing 5% H_2 – 95%-Ar gas mixture. The calculated values of linear thermal expansion coefficients (TECs) are listed in Table 1. The dilatometric curves are smooth, which indicates an absence of first-order phase transitions in the studied temperature

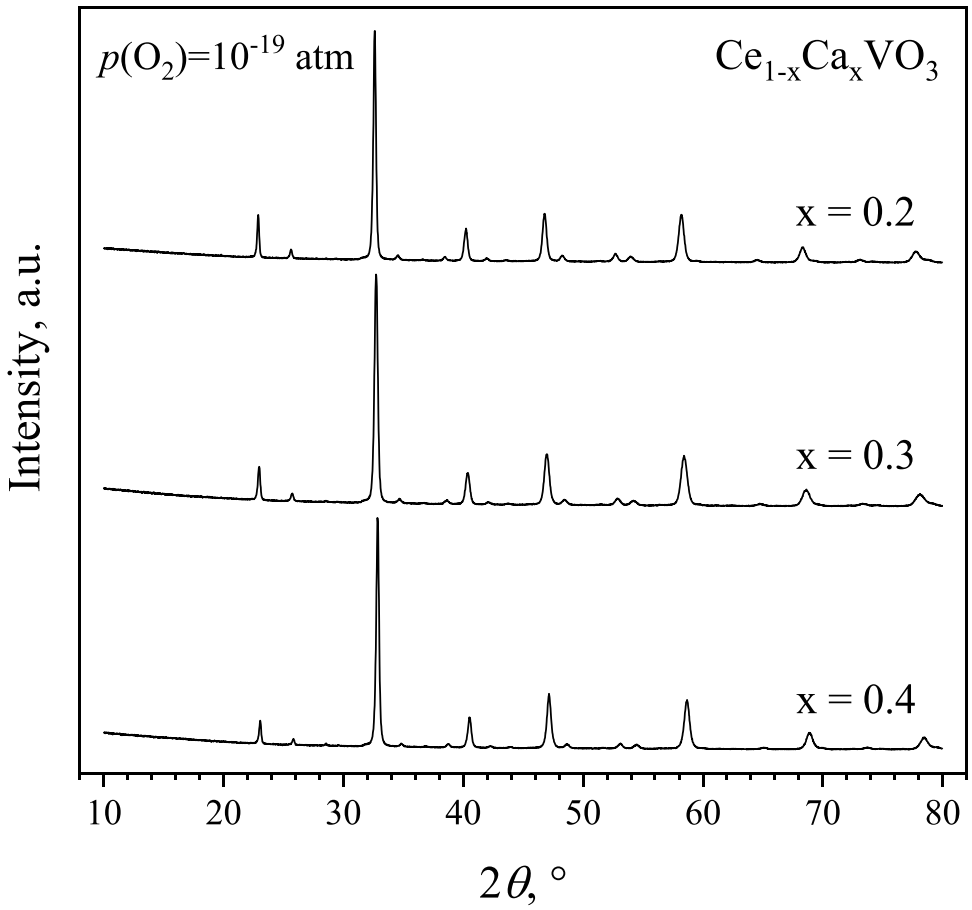

Fig. 2 XRD patterns of $Ce_{1-x}Ca_xVO_3$ powders after annealing in 5% H_2– 3% H_2O-Ar gas mixture at 1123 K

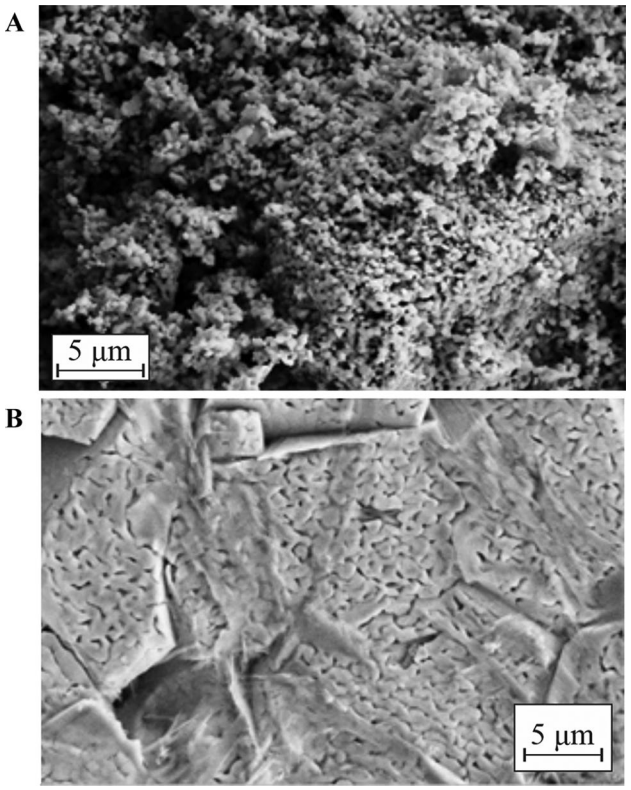

Fig. 3 SEM images of as-synthesized powder (**A**) and fractured ceramics (**B**) of $Ce_{0.7}Ca_{0.3}VO_4$

range. At atmospheric oxygen pressure, the TECs vary in the range $(6.6–9.9)\times10^{-6}$ K^{-1}, increasing with temperature and calcium additions. This tendency may originate from a continuous partial reduction of Ce^{4+} cations on heating. The perovskite-type metavanadates exhibit a higher thermal expansion with respect to their zircon-type analogues (Fig. 6). For instance, in the case of $Ce_{0.8}Ca_{0.2}VO_3$, the

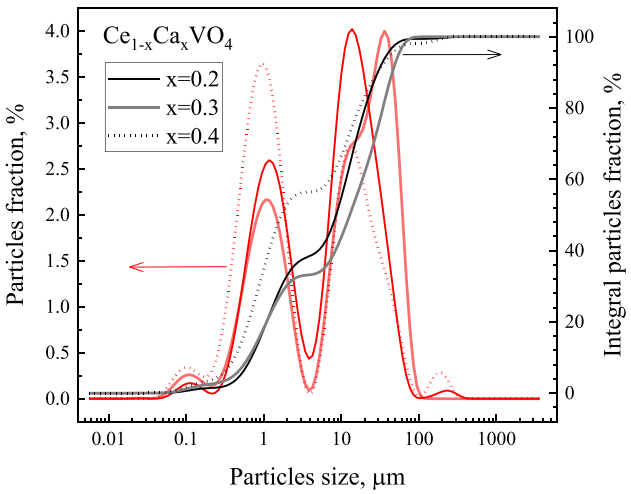

Fig. 4 Particle size distribution in the as-synthesized vanadate powders

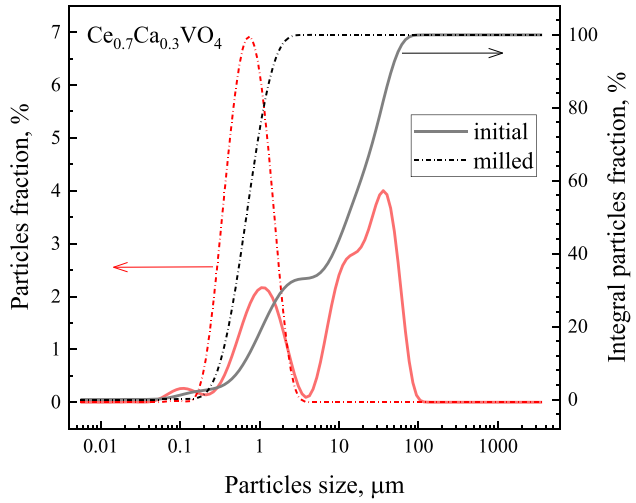

Fig. 5 Comparison of the particle size distributions before and after ball-milling

TEC values are $(9.67\pm0.07)\times10^{-6}$ K^{-1} at 393–853 K and $(11.08\pm0.06)\times10^{-6}$ K^{-1} at 853–1123 K. These values are very close to those of solid electrolytes based on stabilized zirconia, $(10–11)\times10^{-6}$ K^{-1} [18].

Temperature dependencies of the total electrical conductivity (σ) of $Ce_{1-x}Ca_xVO_{4\pm\delta}$ under oxidizing and reducing conditions are shown in Fig. 7. In air, increasing calcium concentration in $Ce_{1-x}Ca_xVO_4$ results in a slight decrease of the conductivity, predominantly electronic. The σ values and the corresponding activation energies (Table 1) are, however, quite similar to one another for all zircon-type orthovanadates. After the transition of $Ce_{1-x}Ca_xVO_4$ into perovskite phase in humidified 5% hydrogen, the conductivity becomes drastically higher, by 2–3 orders of magnitude depending

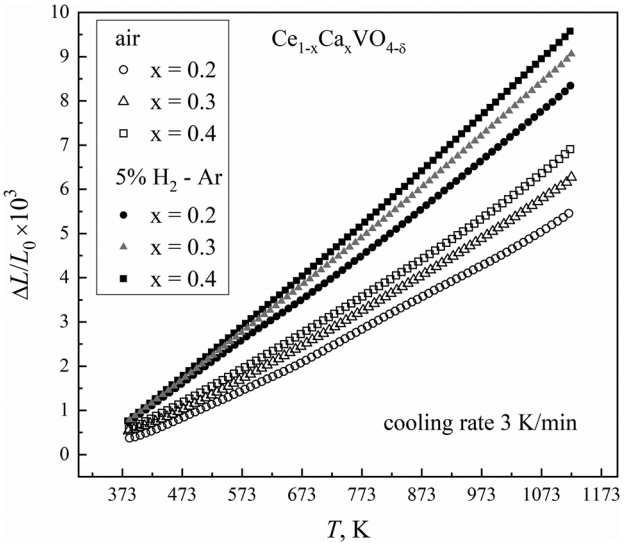

Fig. 6 Dilatometric curves of $Ce_{1-x}Ca_xVO_{4\pm\delta}$ ceramics, collected on cooling in flowing air and 5% H_2 – 95%-Ar gas mixture

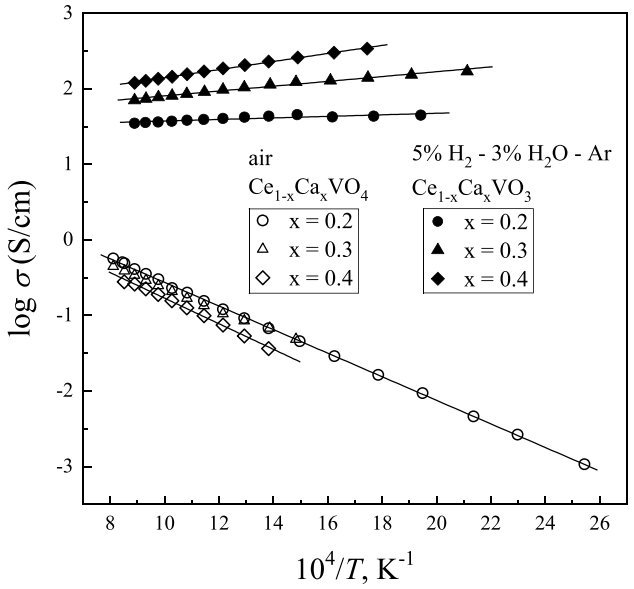

Fig. 7 Temperature dependencies of the total electrical conductivity of $Ce_{1-x}Ca_xVO_{4\pm\delta}$ in oxidizing and reducing atmospheres

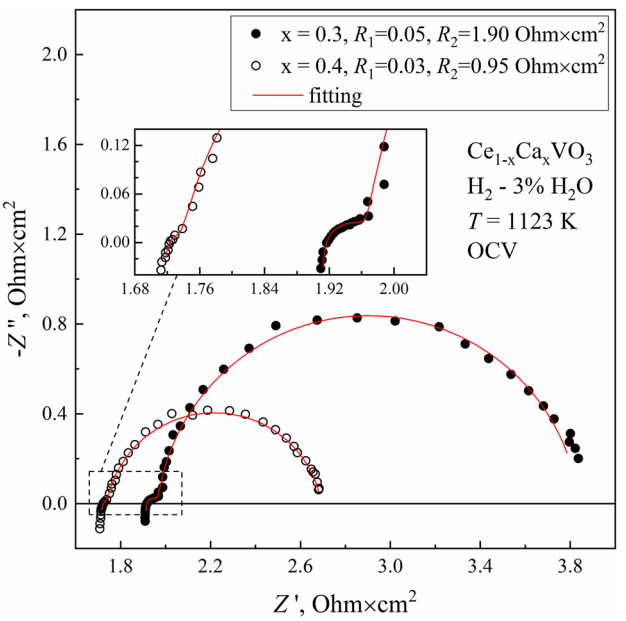

Fig. 8 Impedance spectra of $Ce_{0.7}Ca_{0.3}VO_3$ and $Ce_{0.6}Ca_{0.4}VO_3$ electrode layers in contact with 10Sc1YSZ solid electrolyte and GDC10 protective interlayer under open-circuit conditions in humidified hydrogen at 1123 K

on the composition and temperature. Such an increase is associated with the formation of $V^{3+/4+}$ cations and continuous 3D network of V – O – V bonds, which facilitates electron transfer and delocalization in the perovskite lattice. The conductivity of $Ce_{1-x}Ca_xVO_3$ exhibits so-called pseudo-metallic behavior with a weak temperature dependence, and increases with increasing x. Similar trends are well known for other perovskite-like vanadates, such as $Ln_{1-x}A_xVO_3$ (Ln = La, Nd; A = Ca, Sr; $x > 0.2$), see [19, 20] and references therein. Their origin is related to the appearance of V^{4+} states charge-compensating the substitution of Ce^{3+} with Ca^{2+} and to charge-carrier delocalization. Notice that another charge-compensation mechanism via the oxygen-vacancy formation also cannot be excluded in the present case, but its dominant role would have no effect on the concentration of electronic charge carriers and would decrease electron mobility when Ca^{2+} concentration increases. It should be separately mentioned that the observed level of electronic transport is considerably higher than that reported in the literature [13, 14], which may result from a slow kinetics of phase transition and/or different microstructures of the ceramic materials. For $Ce_{0.6}Ca_{0.4}VO_3$, the conductivity under reducing conditions is as high as 120 S/cm at 1123 K, sufficient for using this material as a component of SOFC anode/SOEC cathode.

Figure 8 displays selected examples of the impedance spectra of $Ce_{0.7}Ca_{0.3}VO_3$ and $Ce_{0.6}Ca_{0.4}VO_3$ electrode layers in contact with 10Sc1YSZ solid electrolyte and GDC10 protective interlayer in flowing humidified H_2, recorded under open-circuit conditions at 1123 K. The spectra consist of two separable arcs where the high-frequency signal is much smaller than the low-frequency one. These signals are usually attributed to a limiting charge transfer process and diffusion processes, respectively [21, 22]. Whatever the microscopic mechanisms, both contributions decrease on Ca doping; the total polarization resistance of $Ce_{0.6}Ca_{0.4}VO_3$ electrode under open-circuit conditions is approximately 1 Ohm × cm^2. The electrode polarization curves at 1123 K are presented in Fig. 9. In correlation

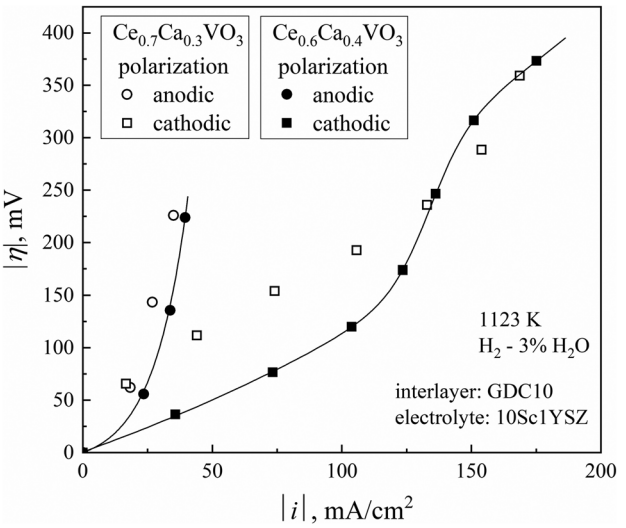

Fig. 9 Dependencies of the overpotentials of $Ce_{0.7}Ca_{0.3}VO_3$ and $Ce_{0.6}Ca_{0.4}VO_3$ porous electrodes on the anodic and cathodic current density in flowing H_2-H_2O at 1123 K

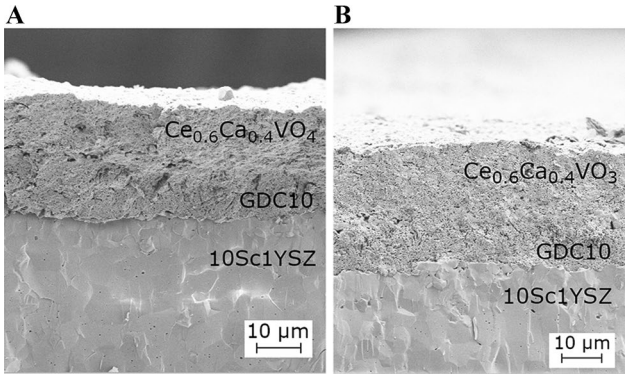

Fig. 10 Cross section of the fractured electrochemical cell with porous $Ce_{0.6}Ca_{0.4}VO_3$ electrode layer in contact with GDC10 interlayer deposited onto the surface of 10Sc1YSZ solid electrolyte, before (**A**) and after (**B**) electrochemical measurements under cathodic polarization conditions

with the conductivity variations (Fig. 7), the overpotentials of $Ce_{0.6}Ca_{0.4}VO_3$ electrode are significantly lower than those of $Ce_{0.7}Ca_{0.3}VO_3$ both under anodic (SOFC mode) and cathodic polarization (SOEC mode). The level of the electrode performance is typical for all-ceramic SOFC anodes [23]. In particular, the overpotentials of $Ce_{0.6}Ca_{0.4}VO_3$ are comparable to those of (La, Sr)VO_3—YSZ [24] and $Ce_{0.7}Sr_{0.3}VO_3$—YSZ [7] composite electrodes. When comparing the anodic and cathodic polarization curves, one may conclude that the $Ce_{1-x}Ca_xVO_3$ electrodes are more active for the water electrolysis process than for hydrogen oxidation. Again, this difference may correlate with variations of electronic transport under the cathodic reduction and anodic oxidation conditions, respectively. Another observation supporting this assumption refers to a relatively fast degradation of the electrode performance under anodic polarization. Most likely, this behavior originates from increasing oxygen chemical potential at the electrode surface, leading to the conductivity decrease and local transformation of perovskite into the zircon-type polymorph. In general, these results show that possible applications of doped cerium vanadates as SOEC cathode components are preferable with respect to the SOFC anodes.

Figure 10 displays one SEM image of the fractured electrochemical cell with porous $Ce_{0.6}Ca_{0.4}VO_3$ electrode after cathodic polarization tests. No evidence of significant microstructural degradation can be found. The electrode layer and protective interlayer retain homogeneous microstructures without traces of cracking or delamination. At the same time, further optimization of the electrode microstructure in order to increase porosity seems necessary.

Conclusions

Cerium-calcium orthovanadates $Ce_{1-x}Ca_xVO_4$ ($x = 0.2$–0.4) with the zircon-type structure were prepared via nitrate-citrate synthesis route and subsequent annealing in air. Doping with calcium leads to moderate unit-cell volume contraction and to a minor decrease in the total electrical conductivity at atmospheric oxygen pressure when the dominant oxidation states of cerium and vanadium cations are 3+/4+ and 5+, respectively. The average linear thermal expansion coefficients of vanadate ceramics in air vary in the range $(6.6–9.9)\times10^{-6}$ K^{-1} at 393–1123 K, increasing with temperature and calcium additions. On reduction, zircon-type phases transform into perovskite-like $Ce_{1-x}Ca_xVO_3$ where Ce^{3+} and $V^{3+/4+}$ states are dominant. This transition is accompanied by a 32% lattice contraction, increasing TECs and a drastic (2–3 orders of magnitude) increase of the electrical conductivity. The reduced materials remain thermomechanically compatible with common solid oxide electrolytes. For instance, in 5% H_2 – 95% Ar atmosphere, the TEC values of $Ce_{0.8}Ca_{0.2}VO_3$ ceramics are $(9.67\pm0.07)\times10^{-6}$ K^{-1} at 393–853 K and $(11.08\pm0.06)\times10^{-6}$ K^{-1} at 853–1123 K. The substitution of cerium with calcium in $Ce_{1-x}Ca_xVO_3$ increases electronic transport and decreases electrode polarization resistance in reducing atmospheres. The latter is lower under cathodic polarization with respect to anodic conditions, presumably due to electronic conductivity variations. Doped cerium vanadates are promising as catalytically active additives to the electrodes of solid oxide fuel and electrolysis cells.

Funding This study received financial support from the Russian Science Foundation (grant 20–19-00478).

References

1. Matsuzaki Y, Yasuda I (2000) The poisoning effect of sulfur-containing impurity gas on a SOFC anode: Part I. Dependence on temperature, time, and impurity concentration. Solid State Ionics 132:261–269. https://doi.org/10.1016/S0167-2738(00)00653-6
2. Cheng Z, Zha S, Aguilar L, Wang D, Winnick J, Liu M (2006) A solid oxide fuel cell running on H_2S/CH_4 fuel mixtures. Electrochem Solid-State Lett 9:2005–2007. https://doi.org/10.1149/1.2137467
3. Cooper M, Channa K, Silva R, Bayless DJ (2010) Comparison of LSV/YSZ and LSV/GDC SOFC anode performance in coal syngas containing H_2S. J Electrochem Soc 157:B1713. https://doi.org/10.1149/1.3489380
4. Danilovic N, Luo JL, Chuang KT, Sanger AR (2009) $Ce_{0.9}Sr_{0.1}VO_x$ (x= 3, 4) as anode materials for H_2S-containing CH_4 fueled solid oxide fuel cells. J Power Sources 192:247–257. https://doi.org/10.1016/j.jpowsour.2009.03.045
5. Petit CTG, Lan R, Cowin PI, Tao Sh (2010) Structure and conductivity of strontium-doped cerium orthovanadates $Ce_{1-x}Sr_xVO_4$

(0≤x≤0.175). J Solid State Chem 183:1231–1238. https://doi.org/10.1016/j.jssc.2010.03.032
6. Reiichi C, Bunichi Y, Yoji S, Yoshitaka T, Masayasu A. Japanese patent - P2004186148A
7. Adijanto L, Padmanabhan VB, Holmes KJ, Gorte RJ, Vohs JM (2012) Physical and electrochemical properties of alkaline earth doped, rare earth vanadates. J Solid State Chem 190:12–17. https://doi.org/10.1016/j.jssc.2012.01.065
8. Tsipis EV, Patrakeev MV, Kharton VV, Vyshatko NP, Frade JR (2002) Ionic and p-type electronic transport in zircon-type $Ce_{1-x}A_xVO_{4-\delta}$ (A= Ca, Sr). J Mater Chem 12:3738–3745. https://doi.org/10.1039/B206004C
9. Tsipis EV, Kharton VV, Vyshatko NP, Shaula AL, Frade JR (2003) Stability and oxygen ionic conductivity of zircon-type $Ce_{1-x}A_xVO_{4+\delta}$ (A=Ca, Sr). J Solid State Chem 176:47–56. https://doi.org/10.1016/S0022-4596(03)00342-6
10. Tsipis EV, Kharton VV, Frade JR (2005) Mixed conducting components of solid oxide fuel cell anodes. J Eur Ceram Soc 25:2623–2626. https://doi.org/10.1016/j.jeurceramsoc.2005.03.114
11. Yokokawa H, Sakai N, Kawada T, Dokiy M (1990) Chemical potential diagrams for rare earth-transition metal-oxygen systems: I, Ln-V-O and Ln-Mn-O system. J Am Ceram Soc 73:649–658. https://doi.org/10.1111/j.1151-2916.1990.tb06567.x
12. Da Silva JLF, Ganduglia-Pirovano MV, Sauer J (2007) Formation of the cerium orthovanadate $CeVO_4$: DFT+U study. Phys Rev B 76: 125117. https://doi.org/10.1103/PhysRevB.76.125117
13. Petit CTG, Lan R, Cowin PI, Irvine JTS, Tao Sh (2011) Structure, conductivity and redox reversibility of Ca-doped cerium metavanadate. J Mater Chem 21:8854–8861. https://doi.org/10.1039/c1jm10960j
14. Petit CTG, Lan R, Cowin PI, Kraft A, Tao Sh (2011) Structure, conductivity and redox stability of solid solution $Ce_{1-x}Ca_xVO_4$ ($0\leq x\leq 0.4125$). J Mater Sci 46:316–326. https://doi.org/10.1007/s10853-010-4812-x
15. Watanabe A (2000) Highly conductive oxides, $CeVO_4$, $Ce_{1-x}M_xVO_{4-0.5x}$ (M= Ca, Sr, Pb) and $Ce_{1-y}Bi_yVO_4$, with zircon-type structure prepared by solid-state reaction in air. J Solid State Chem 153:174–179. https://doi.org/10.1006/jssc.2000.8773
16. Shannon RD (1976) Revised effective ionic radii and systematic studies of interatomic distances in halides and chalcogenides. Acta Cryst A32:751–767. https://doi.org/10.1107/s0567739476001551
17. Shen Y, Huang Y, Sujuan Zheng S, Xuefeng Guo X, Chen Z-X, Luming Peng L, Ding W (2011) Nanocrystals of $CeVO_4$ doped by metallic heteroions. Inorg Chem 50:6189–6194. https://doi.org/10.1021/ic200459t
18. Kharton VV, Marques FMB, Atkinson A (2004) Transport properties of solid oxide electrolyte ceramics: a brief review. Solid State Ionics 174:135–149. https://doi.org/10.1016/j.ssi.2004.06.015
19. Bazuev GV, Shveikin GP (1985) Complex oxides of elements with completing d- and f-shells. Nauka, Moscow (**[in Russian]**)
20. Webb JB, Sayer M (1976) High-temperature transport in lanthanum strontium vanadate. J Phys C: Solid State Phys 9:4151. https://doi.org/10.1088/0022-3719/9/22/011
21. Liu G, Yang Y, Lu X, Qi F, Liang Y, Trukhanov A, Wu Y, Sun Z, Lu X (2022) Fully active bimetallic phosphide $Zn_{0.5}Ge_{0.5}P$: a novel high-performance anode for Na-ion batteries coupled with diglyme-based electrolyte. ACS Appl Mater Interfaces 14:31803–31813. https://doi.org/10.1021/acsami.2c03813
22. Liang Y, Chen Y, Ke X, Zhang Z, Wu W, Lin G, Shi Z (2020) Coupling of triporosity and strong Au-Li interaction to enable dendrite-free lithium plating/stripping for long-life lithium metal anodes. J Mater Chem A 8:18094–18105. https://doi.org/10.1039/d0ta04768f
23. Tsipis EV, Kharton VV (2011) Electrode materials and reaction mechanisms in solid oxide fuel cells: a brief review. III. Recent trends and selected methodological aspects. J Solid State Electrochem 15:1007–1040. https://doi.org/10.1007/s10008-011-1341-8
24. Ge XM, Chan SH (2009) Lanthanum strontium vanadate as potential anodes for solid oxide fuel cells. J Electrochem Soc 156:B386–B391. https://doi.org/10.1149/1.3058585